8.7 Generalized Covariance Functions for Mesoscale Wind Analysis and Data Assimilation

Qin Xu[1*], Kang Nai[1,2] and Li Wei[2]

[1]NOAA/National Severe Storms Laboratory, Norman, Oklahoma
[2]Cooperative Institute for Mesoscale Meteorological Studies, University of Oklahoma

1. Introduction

The streamfunction ψ and velocity potential χ have been widely used as independent control variables in operational variational data assimilation systems on large and synoptic scales. For mesoscale data assimilation, the use of (ψ, χ) often degrades the analyses, so (u, v) have been used in place of (ψ, χ) in the ARPS 3DVar (Gao et al. 1999). The degradations caused by using (ψ, χ) were examined with the WRFVar (Sun et al. 2016), but reasons for the degradations were largely unexplored. Theoretically, if the random vector field of horizontal velocity error is homogenous and isotropic as assumed in 3DVar, then its associated ψ and χ are uncorrelated but u and v are not. This theoretical consideration favors the use of (ψ, χ) over (u, v), but the conventionally used Gaussian covariance functions need to be be modified and generalized in 3DVar for mesoscale wind analysis and data assimilation. The related issues are examined in this paper.

2. Covariance functions in 3DVar for wind analyses

The covariance of background wind errors that involves two points, say, $\mathbf{x}_\mathrm{i} = (x_\mathrm{i}, y_\mathrm{i})$ and $\mathbf{x}_\mathrm{j} = (x_\mathrm{j}, y_\mathrm{j})$ on a vertical level is a second-order tensor function denoted and defined by

$$\mathbf{C}_{\mathbf{vv}}(\mathbf{x}_\mathrm{i}, \mathbf{x}_\mathrm{j}) \equiv <\mathbf{v}_\mathrm{i}\mathbf{v}_\mathrm{j}^\mathrm{T}>, \tag{1}$$

where <( )> denotes the statistical mean of ( ), $\mathbf{v}_\mathrm{i}$ is the background wind error of zero mean at $\mathbf{x}_\mathrm{i}$, and $( )^\mathrm{T}$ denotes the transpose of ( ). Projecting $\mathbf{v}_\mathrm{i}$ onto the l-direction along $\mathbf{r} = \mathbf{x}_\mathrm{j} - \mathbf{x}_\mathrm{i}$ (see the blue arrow in Fig. 1) and onto the t-direction perpendicular to $\mathbf{r}$ with positive to the left, the resulting components are denoted by l_i and t_i, respectively (see Fig. 1). These two components are related to $\mathbf{v}_\mathrm{i} = (u_\mathrm{i}, v_\mathrm{i})^\mathrm{T}$ by $(l_\mathrm{i}, t_\mathrm{i})^\mathrm{T} = \mathbf{R}\mathbf{v}_\mathrm{i}$ where $\mathbf{R} = \mathbf{R}(\alpha)$ is the rotational matrix that rotates the x-axis to the l-direction and $\alpha \equiv \tan^{-1}[(y_\mathrm{j} - y_\mathrm{i})/(x_\mathrm{j} - x_\mathrm{i})]$ is the angle of the rotation, measured positively counterclockwise.

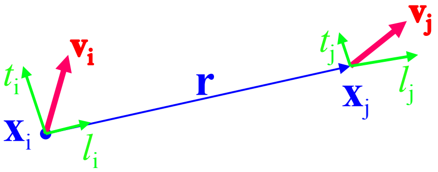

Fig. 1. $\mathbf{v}_\mathrm{i}$ and $\mathbf{v}_\mathrm{j}$ (shown by red arrows), their l-components (green arrows labeled by l_i and l_j) and t-components (green arrows labeled by t_i and t_j).

In 3DVar, the random vector field of $\mathbf{v}_\mathrm{i}$ (or $\mathbf{v}_\mathrm{i}$ normalized by its standard deviation σ if σ is a function of $\mathbf{x}$) is assumed to be homogenous and isotropic. In this case, $C_{lt} \equiv <l_\mathrm{i}t_\mathrm{j}> = C_{tl} \equiv <t_\mathrm{i}l_\mathrm{j}> = 0$, and $\mathbf{C}_{\mathbf{vv}}$ can be transformed into the following canonical form:

$$(C_{ll}, C_{tt})^\mathrm{diag} = \mathbf{R}^\mathrm{T}\mathbf{C}_{\mathbf{vv}}\mathbf{R}, \tag{2}$$

where $C_{ll} \equiv <l_\mathrm{i}l_\mathrm{j}>$ and $C_{tt} \equiv <t_\mathrm{i}t_\mathrm{j}>$ are functions of $r = |\mathbf{r}|$ only. This canonical form is invariant with respect to translations and rotations of the system of points $\mathbf{x}_\mathrm{i}$ and $\mathbf{x}_\mathrm{j}$. As shown in (5.2.23)-(5.2.24) of Daley 1991, C_{ll} and C_{tt} are related to $C_{\psi\psi} \equiv <\psi_\mathrm{i}\psi_\mathrm{j}>$ and $C_{\chi\chi} \equiv <\chi_\mathrm{i}\chi_\mathrm{j}>$ by

$$\begin{aligned} C_{tt} &= -(\partial_r^{\,2}C_{\psi\psi} + r^{-1}\partial_r C_{\chi\chi}), \\ C_{ll} &= -(r^{-1}\partial_r C_{\psi\psi} + \partial_r^{\,2}C_{\chi\chi}). \end{aligned} \tag{3}$$

By partitioning $\mathbf{v}$ into a rotational (or non-divergent) part defined by $\mathbf{v}^\mathrm{r} \equiv (-\partial_y\psi, \partial_x\psi)^\mathrm{T}$ and a divergent part defined by $\mathbf{v}^\mathrm{d} \equiv (-\partial_x\chi, \partial_y\chi)^\mathrm{T}$, we have $<\mathbf{v}^\mathrm{r}_\mathrm{i}\mathbf{v}^{\mathrm{d}\,\mathrm{T}}_\mathrm{j}> = <\mathbf{v}^\mathrm{d}_\mathrm{i}\mathbf{v}^{\mathrm{r}\,\mathrm{T}}_\mathrm{j}> = 0$ and thus $\mathbf{C}_{\mathbf{vv}} = \mathbf{C}^\mathrm{r} + \mathbf{C}^\mathrm{d}$ where $\mathbf{C}^\mathrm{r} \equiv <\mathbf{v}^\mathrm{r}_\mathrm{i}\mathbf{v}^{\mathrm{r}\,\mathrm{T}}_\mathrm{j}>$ and $\mathbf{C}^\mathrm{d} \equiv <\mathbf{v}^\mathrm{d}_\mathrm{i}\mathbf{v}^{\mathrm{d}\,\mathrm{T}}_\mathrm{j}>$. As shown in (2.14) of Xu and Wei (2001), the traces of $\mathbf{C}^\mathrm{r}$ and $\mathbf{C}^\mathrm{d}$ are related to $C_{\psi\psi}$ and $C_{\chi\chi}$ by

$$C_\mathrm{r} \equiv \mathrm{Tr}(\mathbf{C}^\mathrm{r}) = -(\partial_r^{\,2} + r^{-1}\partial_r)C_{\psi\psi} \equiv -\nabla^2 C_{\psi\psi}$$

$$\text{and} \quad C_\mathrm{d} \equiv \mathrm{Tr}(\mathbf{C}^\mathrm{d}) = -(r^{-1}\partial_r + \partial_r^{\,2})C_{\chi\chi} \equiv -\nabla^2 C_{\chi\chi}, \tag{4}$$

respectively, where Tr( ) denotes the trace of ( ).

When $C_{\psi\psi}$ and $C_{\chi\chi}$ are modeled by Gaussian functions (with their associated operators mimicked by recursive filters), $\partial_r^{\,2}C_{\psi\psi}$ and $\partial_r^{\,2}C_{\chi\chi}$ contain negative sidelobes and so do the components of $\mathbf{C}_{\mathbf{vv}}$. This is shown by the exemples in the following two cases.

Case-1. For $C_{\psi\psi} = C_{\chi\chi} \propto \exp[-r^2/(2L^2)]$, we have $C_{uv} = C_{vu} = 0$ and $C_{uu} = C_{vv} = C_{ll} = C_{tt} = -\nabla^2 C_{\psi\psi}$. In this case, $C_{uu} = -\nabla^2 C_{\psi\psi}$ contains a negative sidelobe on each side for $r > 1.5L$ as shown in Fig. 2.

Case-2. For $C_{\psi\psi} \neq C_{\chi\chi}$, we have $C_{uv} = -C_{vu} \neq 0$ and C_{vu} is 90°-rotated C_{uv}, $C_{uu} \neq C_{vv}$ but C_{vv} is 90°-rotated C_{uu}. In this case, C_{uu} contains negative sidelobes as shown in Fig. 3 for $C_{\psi\psi} = 2C_{\chi\chi}$.

---

* Corresponding author address: Qin Xu, National Severe Storms Laboratory, 120 David L. Boren Blvd., Norman, OK 73072-7326; E-mail: Qin.Xu@noaa.gov

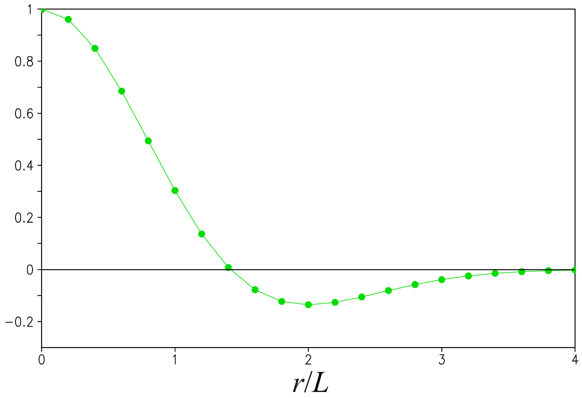

Fig. 2. Normalized function form of $C_{uu}(r)$ (= $-\nabla^2 C_{\psi\psi}$), that is, $C_{uu}(r)/C_{uu}(0)$ for case-1 with $C_{\psi\psi} = C_{\chi\chi} \propto \exp[-r^2/(2L^2)]$.

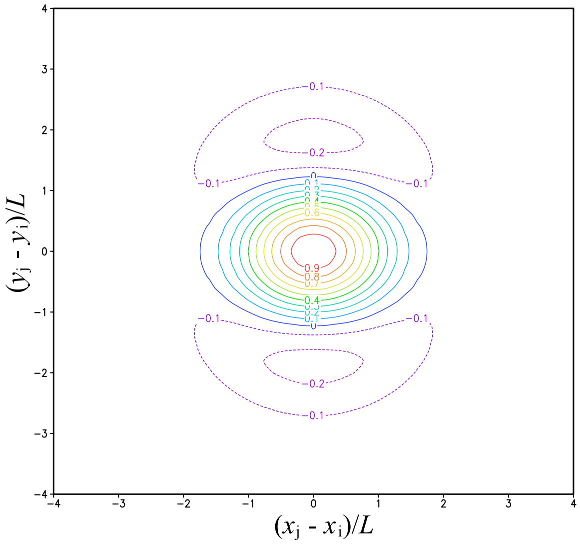

Fig. 3. Contours of $C_{uu}(\mathbf{r})/C_{uu}(0)$ for case-2 with $C_{\psi\psi} = 2C_{\chi\chi} \propto \exp[-r^2/(2L^2)]$.

Negative sidelobes in $C_{tt} \equiv <t_i t_j>$ on the synoptic scale reflect background wind error structures associated with baroclinic waves. A schematic illustration of this is given in Fig. 4, where the background winds associated with the baroclinic wave are assumed to be overpredicted, so the background wind errors largely follow the same directions of their associated true winds and their t-components at $\mathbf{x}_i$ and $\mathbf{x}_j$ are thus negatively correlated as shown by the two green arrows (denoted by t_i and t_j). Similarly, if the baroclinic wave are underpredicted, then the background wind errors will be largely opposite to the directions of their associated true winds, so the two green arrows in Fig. 4 will both reverse their directions and thus the two t-components, t_i and t_j, will be still negatively correlated.

Negative sidelobes in C_{tt} on the synoptic scale are also revealed by C_{tt} estimated from radiosonde innovations, as shown by the example in Fig. 5.

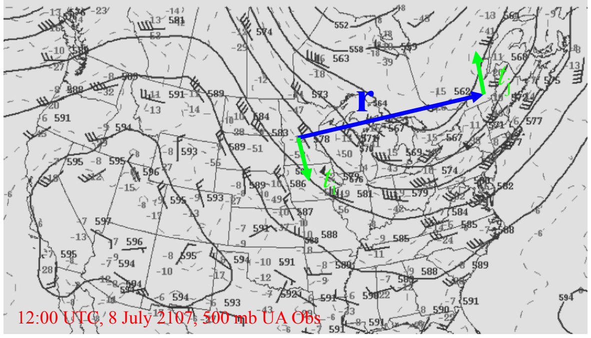

Fig. 4. Schematic illustration of negative correlation between t_i and t_j over the distance of $\mathbf{r}$ (shown by the blue arrow) on the synoptic scale associated with the baroclinic wave on 500 mb.

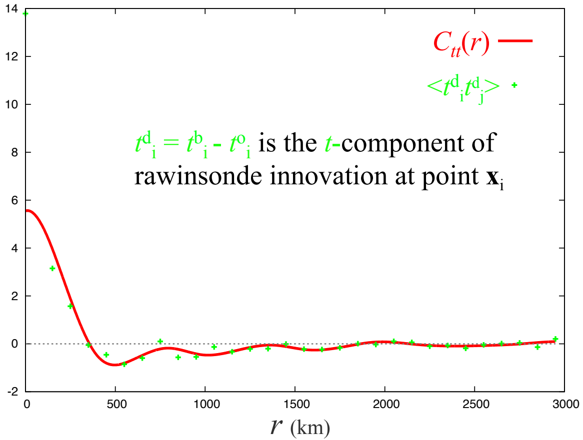

Fig. 5. $C_{tt}(r)$ in m^{2}s^{-2} estimated from binned $<t^d_i t^d_j>$ at 500 mb, where t^d_i (or t^d_i) denotes the rawinsonde innovation (observation minus background) at the i^{th} (or j^{th}) observation point. The background wind error variance is estimated by $C_{tt}(0)$, that is, $C_{tt}(r)|_{r=0}$. The observation error variance is estimated by $<(t^d_i)^2> - C_{tt}(0)$. The data are originally from Fig. 3b of Xu and Wei (2001).

3. Issues in 3DVar on mesoscale wind analyses

Negative sidelobes in C_{tt} and $C_+ \equiv C_{tt} + C_{ll} = \mathrm{Tr}(\mathbf{C}_{\mathbf{vv}})$ have physical and statistical relevance on the synoptic scale (as shown in the previous section) but not on the mesoscale. There should be no negative sidelobe in C_+, C_r or C_d on the mesoscale. This is evidenced by C_+, C_r and C_d estimated from radar radial-wind innovations (Xu et al. 2007a,b), as shown by the examples in Fig. 6.

When ψ and χ are used as control variables in 3DVar with $C_{\psi\psi}$ and $C_{\chi\chi}$ modeled by Gaussian functions, negative sidelobes generated in $C_+(r)$, $C_r(r)$ and $C_d(r)$ can cause spurious features in analyzed winds especially outside and around data covered areas (as often observed in mesoscale wind analyses performed with high-resolution radar wind data). This provides a theoretical explanation for the aforementioned degradations in mesocale wind analyses. It also raises an important issue regarding how to eliminate the negative sidelobes in $C_+(r)$, $C_r(r)$ and $C_d(r)$ in order to use ψ and χ either implicitly or explicitly as control variables in 3DVar for mesocale wind analyses.

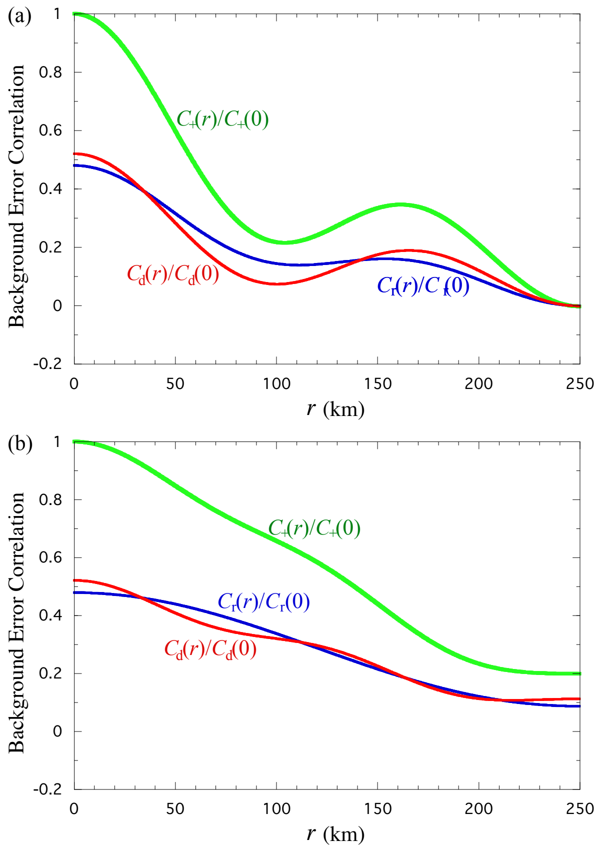

Fig. 6. Normalized $C_+(r)$, $C_\mathrm{r}(r)$ and $C_\mathrm{d}(r)$, that is, $C_+(r)/C_+(0)$, $C_\mathrm{r}(r)/C_\mathrm{r}(0)$ and $C_\mathrm{d}(r)/C_\mathrm{d}(0)$ estimated from radar radial-wind innovations (collected from 6 operational WSR-88D radars in Oklahoma and its vicinity states with the background winds from operational NMM forecasts) for two cases: (a) in the vertical layer between $z = 0.4 \pm 0.2$ km under a clear weather condition on 5/21/2005; (b) in the vertical layer between $z = 0.8 \pm 0.2$ km under a rainy weather condition on 5/23/2005. The data for the clear weather case in panel (a) are originally from Fig. 5 of Xu et al. (2007b). Note that the depressions of the three curves around $r = 100$ km in panel (a) are unreal and unrepresentative as they are caused by date void gaps between different radars (see Fig. 4 of Xu et al. 2007b and the related slide number 7 in the recorded presentation at https://ams.confex.com/ams/22WAF18NWP/webprogram/Paper123419.html).

4. Newly modified covariance functions

To address the issue raised in the previous section, we need to modify the conventional covariance functions reviewed in the previous section. First, we need to transform $\mathbf{C}^\mathrm{r}$ and $\mathbf{C}^\mathrm{d}$ into their respective canonical forms, that is, $(C_{ll}^\mathrm{r}, C_{tt}^\mathrm{r})^\mathrm{diag} = \mathbf{R}^\mathrm{T}\mathbf{C}^\mathrm{r}\mathbf{R}$ and $(C_{ll}^\mathrm{d}, C_{tt}^\mathrm{d})^\mathrm{diag} = \mathbf{R}^\mathrm{T}\mathbf{C}^\mathrm{d}\mathbf{R}$, respectively, similar to that in (2) for $\mathbf{C}_\mathbf{vv}$ (= $\mathbf{C}^\mathrm{r} + \mathbf{C}^\mathrm{d}$). This leads to $(C_{ll}, C_{tt})^\mathrm{diag} = (C_{ll}^\mathrm{r}, C_{tt}^\mathrm{r})^\mathrm{diag} + (C_{ll}^\mathrm{d}, C_{tt}^\mathrm{d})^\mathrm{diag}$, so $(C_{ll}^\mathrm{r}, C_{tt}^\mathrm{r})^\mathrm{diag}$ is the rotational part and $(C_{ll}^\mathrm{d}, C_{tt}^\mathrm{d})^\mathrm{diag}$ is the divergent part of $(C_{ll}, C_{tt})^\mathrm{diag}$.

After the above preparation, the rotational part of $C_{tt}(r)$, that is, $C_{tt}^\mathrm{r}(r) \equiv -\partial_r^2 C_{\psi\psi}$ can be modeled by $\sigma_\mathrm{r}^2 G(r/L_\mathrm{r})$, where

$$G(\ ) \equiv \exp[-(\ )^2/2] \tag{5}$$

denotes the Gaussian function form, σ_r^2 is the error variance for each component of $\mathbf{v}^\mathrm{r}$ and L_r is the de-correlation length scale for $\mathbf{v}^\mathrm{r}$. The rotational part of $C_{ll}(r)$ is then given by $C_{ll}^\mathrm{r}(r) = -r^{-1}\partial_r C_{\psi\psi} = \sigma_\mathrm{r}^2 E(r/L_\mathrm{r})$, where

$$E(r/L_\mathrm{r}) \equiv \int_0^r dr' G(r'/L_\mathrm{r})/r. \tag{6}$$

Similarly, the divergent part of $C_{ll}(r)$, that is, $C_{ll}^\mathrm{d}(r) \equiv -\partial_r^2 C_{\chi\chi}$ can be modeled by $\sigma_\mathrm{d}^2 G(r/L_\mathrm{d})$ where σ_d^2 is the error variance for each component of $\mathbf{v}^\mathrm{d}$ and L_d is the de-correlation length scale for $\mathbf{v}^\mathrm{d}$. The divergent part of $C_{tt}(r)$ is then given by $C_{tt}^\mathrm{d}(r) = -r^{-1}\partial_r C_{\chi\chi} = \sigma_\mathrm{d}^2 E(r/L_\mathrm{d})$.

With the above modifications, we have

$$\begin{aligned} C_{tt}(r) &= C_{tt}^\mathrm{r}(r) + C_{tt}^\mathrm{d}(r) = \sigma_\mathrm{r}^2 G(r/L_\mathrm{r}) + \sigma_\mathrm{d}^2 E(r/L_\mathrm{d}),\\ C_{ll}(r) &= C_{ll}^\mathrm{r}(r) + C_{ll}^\mathrm{d}(r) = \sigma_\mathrm{r}^2 E(r/L_\mathrm{r}) + \sigma_\mathrm{d}^2 G(r/L_\mathrm{d}); \end{aligned} \tag{7}$$

and

$$\begin{aligned} C_\mathrm{r}(r) &= C_{tt}^\mathrm{r}(r) + C_{ll}^\mathrm{r}(r) = \sigma_\mathrm{r}^2[G(r/L_\mathrm{r}) + E(r/L_\mathrm{r})],\\ C_\mathrm{d}(r) &= C_{ll}^\mathrm{d}(r) + C_{tt}^\mathrm{d}(r) = \sigma_\mathrm{d}^2[G(r/L_\mathrm{d}) + E(r/L_\mathrm{d})]. \end{aligned} \tag{8}$$

For C_r (or C_d) in (8) to have the same de-correlation length, defined by $[C_\mathrm{r}(r)|_{r=0}]^{1/2}/[-\nabla^2 C_\mathrm{r}(r)|_{r=0}]^{1/2}$, as the conventional C_r (or C_d) in (4), we need to set L_r (or L_d) $= L(11/32) \approx L/\sqrt{3}$. The detailed derivation of this setting is omitted here. The modified covariance functions in (7)-(8) and their derived C_{uu} and C_{vv} contain no negative sidelobe, as shown by the examples in Figs. 7 and 8 (versus those in Figs. 2 and 3) for the following two cases.

Case-1. For $C_\mathrm{r} = C_\mathrm{d} \propto G(\sqrt{3}r/L) + E(\sqrt{3}r/L_\mathrm{r})$ in (8), we have $C_{uv} = C_{vu} = 0$ and $C_{uu} = C_{vv} = C_{ll} = C_{tt} \propto G(\sqrt{3}r/L) + E(\sqrt{3}r/L)$. In this case, C_{uu} (= C_{vv}) contains no negative sidelobe, as shown in Fig. 7.

Case-2. For $C_\mathrm{r} \neq C_\mathrm{d}$, we have $C_{uv} = -C_{vu} \neq 0$, C_{vu} is still 90° rotated C_{uv}, $C_{uu} \neq C_{vv}$ and C_{vv} is 90° rotated C_{uu}. In this case, neither C_{uu} nor C_{vv} (90°-rotated C_{uu}) has negative sidelobe as shown in Fig. 8 for $C_\mathrm{r} = 2C_\mathrm{d} \propto G(\sqrt{3}r/L) + E(\sqrt{3}r/L)$ in (8).

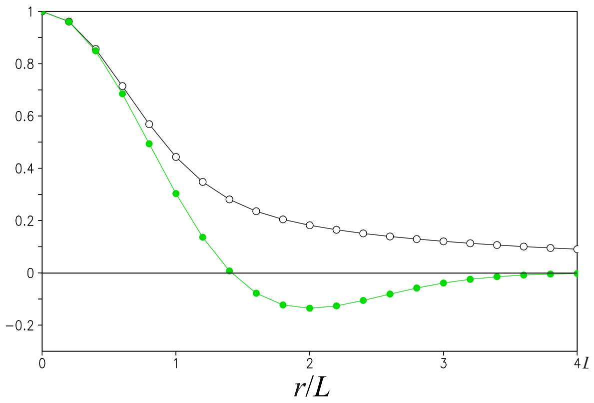

Fig. 7. As in Fig. 2 but with the modified $C_{uu}(r)$ plotted by the black curve with $C_\mathrm{r} = C_\mathrm{d} \propto G(\sqrt{3}r/L) + E(\sqrt{3}r/L)$ in addition to the green curve from Fig. 2 for case 1.

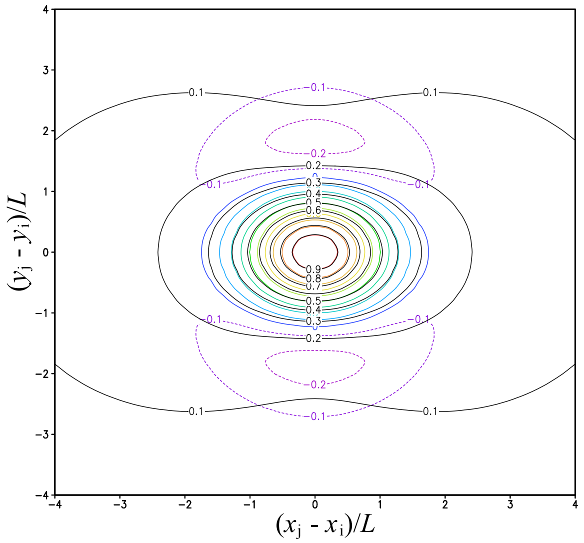

Fig. 8. As in Fig. 3 but with the modified $C_{uu}(\mathbf{r})/C_{uu}(0)$ plotted by the black contours for $C_r = 2C_d \propto G(\sqrt{3}r/L) + E(\sqrt{3}r/L)$ in addition to the color contours from Fig. 3 for case 2.

5. Comparative tests with radar observations

For 3D wind analyses, $C_r(r)$ and $C_d(r)$ in (8) are extended to

$$C_r(r)G(z/H_r) \text{ and } C_d(r)G_2(z_i, z_j), \text{ respectively,} \tag{9}$$

where $G_2(z_i, z_j) = (1 - z_-^2/H_d^2)G(z_-/H_d) + (1 - z_+^2/H_d^2)G(z_+/H_d)$ and $z_\pm = z_j \pm z_i$. C_{tt} and C_{tt} in (7) are also extended accordingly. Similar 3D extensions can be made to the conventional C_r and C_d in (4) and thus C_{tt} and C_{tt} in (3).

To examine whether and how the modified covariance formulations can improve mesoscale wind analyses over the conventional covariance formulations, the conventional and modified formulations are both used to construct the background error covariance matrix for radar wind analyses in a 3DVar formulated similarly to that in Xu et al. (2015) except that the radial-velocity formulation is upgraded to include the vertical velocity. Facilitated by the upgraded radial-velocity formulation and the above 3D extensions of covariance functions, the analyzed 3D winds are ensured to satisfy the mass continuity and surface boundary condition automatically. The detailed formulations are omitted here.

The above 3DVar is applied to radial-velocity super-observations (with a coarsened resolution of 10 km) from the operational KTLX radar for the 20 May 2013 Oklahoma tornadic storm with the background wind field from 1-hour forecast produced by the NCEP operational rapid refresh model (RAP). The horizontal-wind increment field produced by the 3DVar analysis with each type of covariance formulation is shown by the white arrows at z = 2 km in Fig. 9 superimposed on the image of radial-velocity super-innovation (super-observation minus background radial-velocity at each super-observation location) from the KTLX radar at 0.5° tilt.

As shown in each panel of Fig. 9, the radial components of the incremental winds can match quite closely the radial-velocity super-innovations around z = 2 km, that is, around the range circle of 116 km radius (marked by the yellow "•" labeled with "z = 2 km") on the 0.5° tilt. However, the incremental winds in panel (a) are less smooth and diminish more quickly away from the super-innovation covered area than those in panel (b). These are the main differences of the incremental winds in panel (a) from those in panel (b), and these differences are caused by the negative sidelobes in the conventional covariance functions used in panel (a).

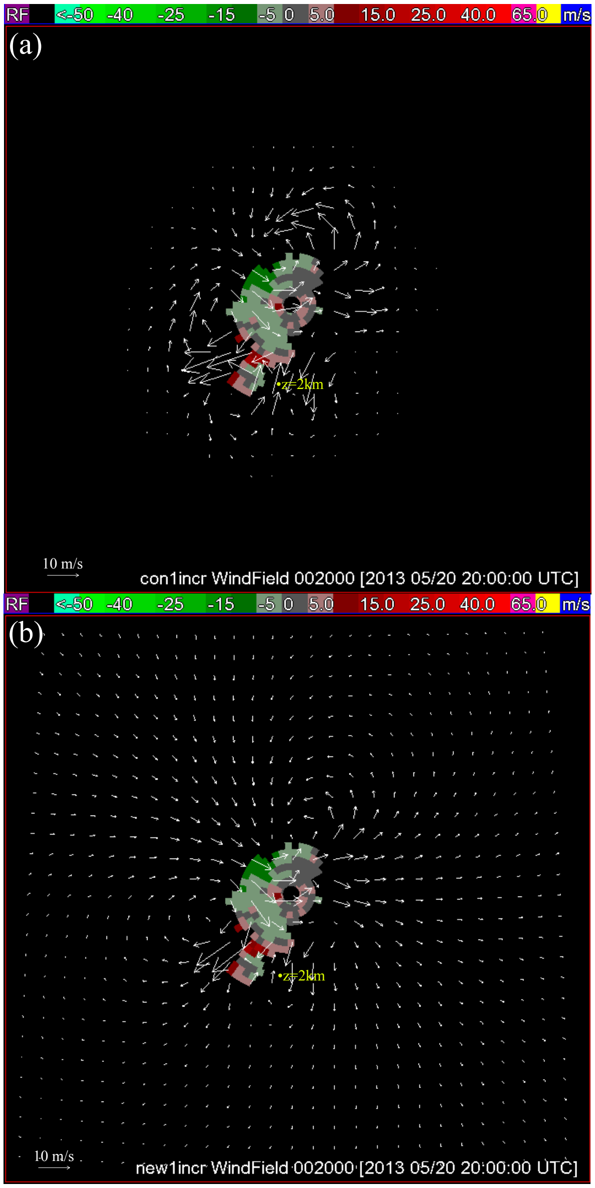

Fig. 9. (a) Horizontal-wind increment field produced by the 3DVar using the conventional covariance formulations [with $C_{\psi\psi}(r) = C_{\chi\chi}(r) \propto G(r/L)$, L = 50 km, and $H_r = H_d = H$ = 0.8 km] plotted at z = 2 km by white arrows superimposed on the images of radial-velocity super-innovation at 0.5° tilt from the operational KTLX radar. (b) As in (a) but using the modified covariance formulations [with $C_r(r) = C_d(r) \propto G(\sqrt{3}r/L)+E(\sqrt{3}r/L)$]. The analysis domain is 800x800x10km with $\Delta x = \Delta y$ = 5 km and Δz = 0.25 km. The color bar on the top of each panel is the velocity scale for the radial-velocity super-innovations.

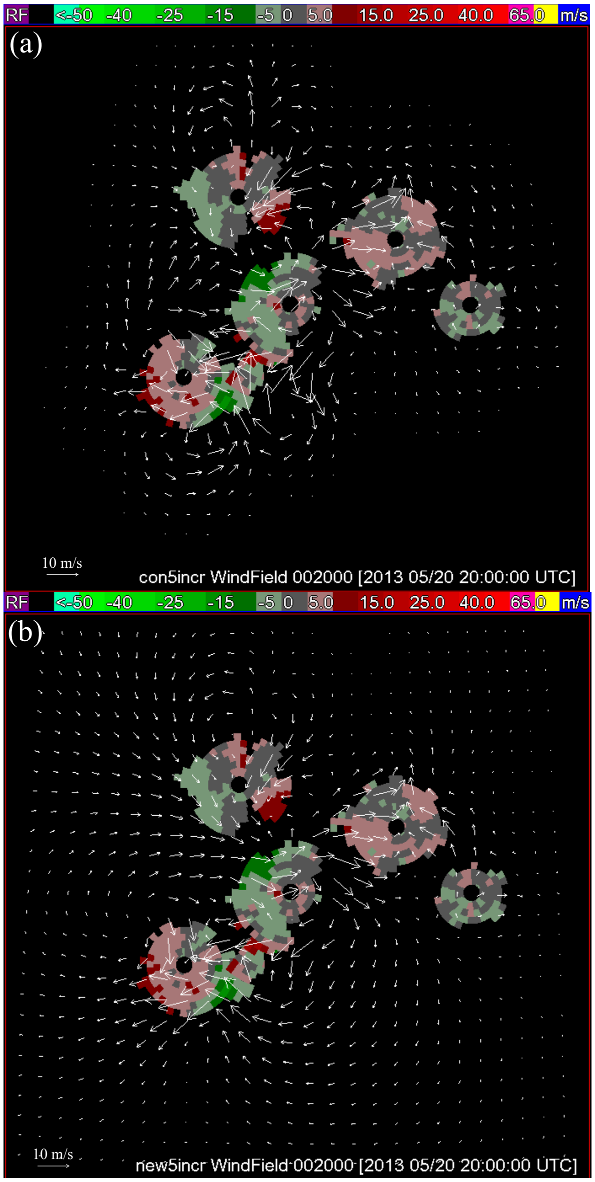

Fig. 10. As in Fig. 9 but with radial-velocity super-innovations from five radars; that is, the operational KFDR, KINX, KVNX and KSRX radars in addition to the KTLX radar.

The above 3DVar is also applied to radial-velocity super-observations from five operational (KTLX, KFDR, KINX, KVNX and KSRX) radars for the same case with the same covariance formulations as in Fig. 9a (or 9b), and its produced horizontal-wind increment field is shown at z = 2 km in Fig. 10a (or 10b) superimposed on the images of radial-velocity super-innovations from the five radars at their respective 0.5° tilts.

The radial-velocity increment field (computed from the 3D wind increment field) produced by the single-Doppler analysis that produces Fig. 9a (or 9b) is plotted by the color contours in Fig. 11a (or 11b). The radial-velocity increment field produced by the five-Doppler analysis that produces Fig. 10a (or 10b) is plotted by black contours in Fig. 11a (or 11b).

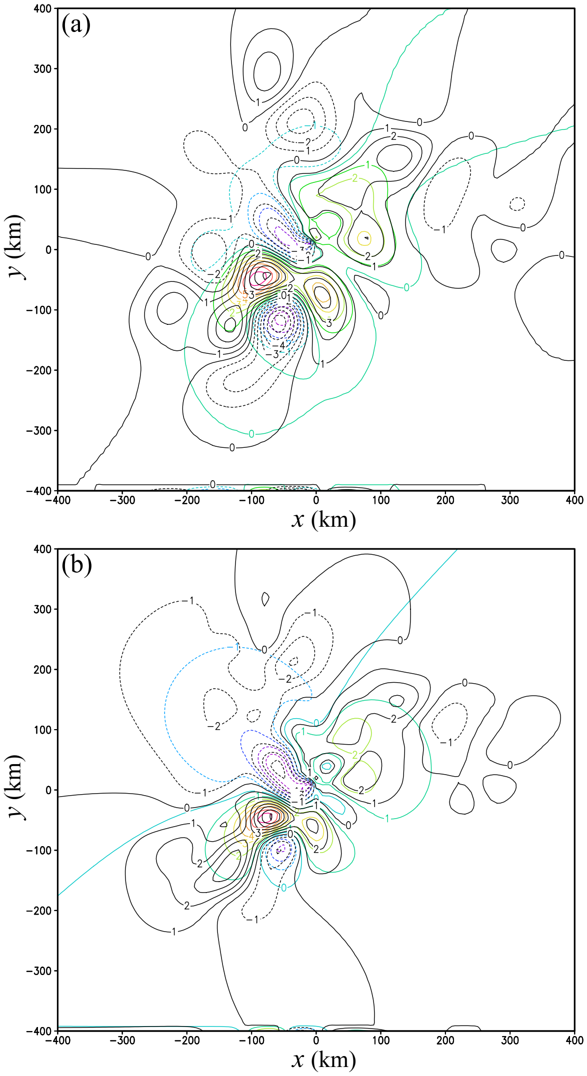

Fig. 11. (a) Radial-velocity increment field (plotted by color contours) at z = 2 km produced by using observations from the KTLX radar only (as shown in Fig. 9a) versus that (plotted by black contours) produced by using observations from the five radars (as shown in Fig. 10a) with the conventional covariance formulations. (b) As in (a) but produced with the modified covariance formulations.

As shown in Fig. 11a for the conventional covariance formulations, the color contours match the black contours closely in the KTLX data covered area (that is, the area covered by the KTLX radial-velocity super-innovations as shown Fig. 9a) but become increasingly different from the black contours beyond the KTLX-covered area. Similar features are seen in Fig. 11b for the modified covariance formulations, but the color contours and the black contours match the KTLX radial-velocity super-innovations more tightly in the KTLX data covered area than those in Fig. 11a, and the color contours match the black contours more closely in and around the KTLX data covered area than those in Fig. 11a.

For quantitative evaluations, the root mean square (RMS) difference between the two radial-velocity increment fields (produced by the single-Doppler and five-Doppler analyses) is computed for each type of covariance formulation in each of the following three areas (that partition the analysis domain at $z = 2$ km).

I. The area covered by the KTLX super-innovations with each super-innovation covering its vicinity volume within the ellipsoid of $a = b = L$ and $c = H$ centered at the super-innovation, where (a, b, c) are the semi-principal axes of the ellipsoid in the space of (x, y, z), and $L = 50$ km (or $H = 0.8$ km) is the de-correlation length (or depth) used in the covariance formulations as described in the caption of Fig. 9.

II. The area influenced by the KTLX super-innovations outside the above area-I with each super-innovation influences its vicinity volume within the ellipsoid of $a = b = 3L$ and $c = 3H$ centered at the super-innovation.

III. The area outside the above area-II.

The above three areas (marked by I, II and III) are shown in Fig. 12. The RMS differences computed in these three areas are listed for each type of covariance formulation in Table 1.

As shown in Table 1, the RMS difference in area-I is reduced by the use of the modified covariance formulations. This reduction can be explained by the fact that the five-Doppler analysis is no longer adversely affected in area-I by the negative sidelobes (in the conventional covariance functions) that negatively and un-physically correlate the analysis increments in area-I to those radial-velocity super-innovations (from the four radars other than the KTLX radar) that are distant from area-I beyond the de-correlation length scale L.

The RMS difference in area-II is also reduced by the use of the modified covariance formulations. This reduction can be explained by the fact that the single-Doppler analysis is no longer adversely affected in area-II by the negative sidelobes (in the conventional covariance functions) that negatively and un-physically correlate the analysis increments in area-II to the KTLX radial-velocity super-innovations that are distant from area-II beyond the de-correlation length scale L.

As shown in Figs. 9 and 11, the horizontal-wind increments and radial-velocity increments produced by the single-Doppler analysis diminish to nearly zero in area-III. Thus, for each type of covariance formulation, the RMS difference in area-III is essentially the RMS value of radial-velocity increments produced by the five-Doppler analysis. This explains why the RMS difference in area-III is not significantly affected by the use of the modified covariance formulations as shown in Table 1.

Table 1. RMS difference in each area for each type of covariance formulation.

Covariance formulations	Conventional	Modified
	RMS difference	RMS difference
Area-I	0.51 $\mathrm{ms^{-1}}$	0.80 $\mathrm{ms^{-1}}$
Area-II	0.87 $\mathrm{ms^{-1}}$	1.35 $\mathrm{ms^{-1}}$
Area-III	0.23 $\mathrm{ms^{-1}}$	0.20 $\mathrm{ms^{-1}}$

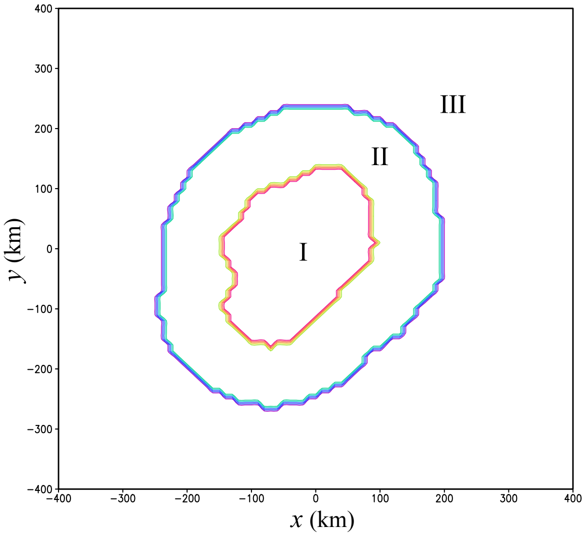

Fig. 12. Three areas (that partition the analysis domain at $z = 2$ km) marked by I, II and III. Area-I is enclosed by the brown contour. Area-II is between the brown and blue contours. Area-III is outside the blue contours,

6. Conclusions

The results presented in this paper can be summarized and highlighted by the following points:

- Conventionally used Gaussian covariance functions for (ψ, χ) cause negative sidelobes in the covariance functions derived for (u, v). Negative sidelobes reflect background wind error structures associated with baroclinic waves on the synoptic scale, but they are unphysical on the mesoscale and can cause spurious features in their analyzed winds outside and around data covered areas.
- Using Gaussian covariance functions for u and v separately and independently can eliminate the aforementioned negative sidelobes, but these covariance formulations are inconsistent with the 3DVar-assumed homogeneity and isotropy for the random vector field of horizontal wind errors unless the rotational and divergent parts of horizontal wind error field are statistically equivalent to each other (with $\mathbf{C}^r = \mathbf{C}^d$).
- The modified covariance functions introduced in (7)-(8) of this paper can eliminate the aforementioned negative sidelobes without the above inconsistency. Their utility in 3DVar and advantages over their conventional counterparts are demonstrated and evaluated by comparative tests with radar radial-velocity observations in section 5.

The modified covariance functions can be used easily to construct the background covariance matrix directly in 3DVar for mesoscale wind analyses, but they are non-Gaussian [as shown in (7)-(9) of this paper] and thus cannot be readily mimicked as operators by the existing recursive filters (designed to mimic Gaussian operators). This problem and related challenging issues need to be addressed in future studies.

Acknowledgments

The research work was supported by the Warn-on-Forecast project at NSSL and the ONR Grants N000141410281 and N000141712375 to the University of Oklahoma (OU).

Funding was also provided to CIMMS by NOAA/Office of Oceanic and Atmospheric Research under NOAA-OU Cooperative Agreement #NA17RJ1227, U.S. Department of Commerce.

REFERENCES

Daley, R. 1991: *Atmospheric data analysis*. Cambridge University Press, New York, 457 pp.

Gao, J., M. Xue, A. Shapiro, and K. K. Droegemeier, 1999: A vari- ational method for the retrieval of three-dimensional wind fields from dual-Doppler radars. Mon. Wea. Rev., 127, 2128–2142.

Sun, J., H. Wang, W. Tong, Y. Zhang, C.-Y. Lin and D. Xu, 2016: Comparison of the impacts of momentum control variables on high-resolution variational data assimilation and precipitation forecasting. *Mon. Wea. Rev.*, **144**, 149–169.

Xu, Q., and L. Wei, 2001: Estimation of three-dimensional error covariances. Part II: Analysis of wind innovation vectors. *Mon. Wea. Rev*., **129**, 2939–2954.

Xu, Q., K. Nai, and L. Wei, 2007a: An innovation method for estimating radar radial-velocity observation error and background wind error covariances. *Quart. J. Roy. Meteor. Soc.*, **133**, 407–415.

Xu, Q., K. Nai, L. Wei, H. Lu, P. Zhang, S. Liu, and D. Parrish, 2007b: Estimating radar wind observation error and NCEP WRF background wind error covariances from radar radial-velocity innovations. Extended Abstract. *18th Conference on Numerical Weather Prediction.* 25-29 June 2007, Park City, UT. Amer. Meteor. Soc., 1B.3.

Xu, Q., L. Wei, K. Nai, S. Liu, R. M. Rabin, and Q. Zhao, 2015: A radar wind analysis system for nowcast applications. *Advances in Meteorology*. vol. **2015**, Article ID 264515, 13 pages.